ACCSCIENCE PUBLISHING

International Journal of Bioprinting

RESEARCH ARTICLE

Coaxial 3D printing of hollow tubular sodium alginate/polyacrylamide double-network hydrogel scaffolds

Wenle Yu[1†], Dingjian Liang[2†], Renzhi Wang[1], Jingyao Gai[1], Quanhui Liu[3], Yuanfen Chen[1*], and Ben Huang[4*]

[1]School of Mechanical Engineering, Guangxi University, Nanning, Guangxi Zhuang Autonomous Region, China

[2]Department of Radiation Oncology, Minzu Hospital of Guangxi Zhuang Autonomous Region, Affiliated Minzu Hospital of Guangxi Medical University, Nanning, Guangxi Zhuang Autonomous Region, China

[3]College of Animal Science and Technology, Guangxi University, Nanning, Guangxi Zhuang Autonomous Region, China

[4]Guangxi Key Laboratory of Eye Health, Department of Technical Support, The People's Hospital of Guangxi Zhuang Autonomous Region, Guangxi Academy of Medical Sciences, Nanning, Guangxi Zhuang Autonomous Region, China

[†]*These authors contributed equally to this work.*

***Corresponding authors:**
Yuanfen Chen (yuanfenchen@gxu.edu.cn);
Ben Huang (bhuang@gxams.org.cn)

Citation: Yu W, Liang D, Wang R, *et al*. Coaxial 3D printing of hollow tubular sodium alginate/polyacrylamide double-network hydrogel scaffolds. *Int J Bioprint.* 2026;12(3):026130119. doi: 10.36922/IJB026130119

Received: March 27, 2026

Revised: April 20, 2026

Accepted: April 24, 2026

Published online: May 4, 2026

Abstract

Tubular hydrogel scaffolds facilitate nutrient and oxygen transport, making them particularly suitable for culturing cells with high metabolic demands. In this study, a double-network hydrogel scaffold with a tubular structure was fabricated using coaxial extrusion-based 3D printing. The hydrogel was composed of sodium alginate and polyacrylamide, and its biocompatibility was assessed through cell culture experiments. The results show that the crosslinking sequence, material composition, and printing parameters were the main factors affecting the macrostructure, microstructure, and mechanical properties of the hydrogel. The CA-PAm hydrogel, in which alginate was ionically crosslinked before subsequent acrylamide (AAm) polymerization under UV exposure, exhibited a more compact microstructure and superior mechanical performance. By optimizing the material composition, the CA-PAm hydrogel achieved a tensile strength of 809.80 kPa and an elongation at break of 217.07%. In addition, the inner-to-outer flow-rate ratio and the platform moving speed are critical factors determining the tubular structural parameters and 3D structural stability. The hydrogel leachate assay showed 89.8% cell viability, and perfusion culture within the tubular scaffold showed an MEF survival rate of 85.4% after three days, indicating good biocompatibility of the scaffold. These results show that crosslinking-sequence reconfiguration is a practical strategy for matching hydrogel network formation with the requirements of coaxial tubular printing and provides a feasible route for fabricating mechanically robust and cytocompatible hollow hydrogel scaffolds for tissue engineering.

Keywords: Coaxial 3D printing; Hollow tubular scaffold; Sodium alginate/polyacrylamide; Double-network hydrogel; Sequential crosslinking

1. Introduction

Tissue engineering is an interdisciplinary field that integrates biology, materials science, chemistry, and engineering. Its primary objective is to fabricate biological scaffolds that provide a three-dimensional microenvironment for cells, thereby supporting the formation of functional tissues for regenerative repair.[1] Accordingly, both scaffold fabrication strategies and scaffold performance are critical to the success of tissue engineering. In particular, for cell culture systems with relatively high mass-transfer demands, scaffolds containing hollow tubular structures are especially attractive because they facilitate the transport of oxygen, nutrients, and metabolic waste.[2-4] In recent years, 3D manufacturing technologies have been increasingly applied in tissue engineering,[5-11] providing efficient and versatile routes for fabricating architectures that are difficult to obtain using conventional methods.[12-16] Among these approaches, extrusion-based coaxial 3D printing has emerged as an effective method for continuously fabricating hollow tubular architectures.[17] For instance, Attalla *et al.*[18] developed a nozzle capable of multi-axis extrusion printing and successfully fabricated patterned multi-layered tubular structures. The channels maintained structural integrity while supporting cell viability and growth. Similarly, Shao *et al.*[19] utilized gelatin methacrylate as a bioink, in which the core gelatin phase provided temporary structural support during printing, and was subsequently dissolved during culture to form hollow tubular structures. Despite these advances, hydrogel-based tubular scaffolds still often suffer from insufficient mechanical robustness and limited structural fidelity, especially when stable hollow geometry and multilayer integration are required simultaneously.

To address the mechanical limitations of conventional hydrogels, double-crosslinked or double-network hydrogels have attracted increasing attention in tissue engineering. For instance, Pei *et al.*[20] developed a microcrystalline cellulose-reinforced polyvinyl alcohol–glycidyl methacrylate double-network hydrogel, in which tannic acid was incorporated as a crosslinking agent to significantly improve both mechanical strength and cytocompatibility. Likewise, E *et al.*[21] fabricated a dual-crosslinked polyvinyl alcohol composite hydrogel reinforced with TEMPO-oxidized cellulose nanofibers and borax. Furthermore, Zhong *et al.*[22] highlighted in a review that the combination of physical and chemical crosslinks in polyvinyl alcohol-based hydrogels can effectively balance elasticity and toughness. Collectively, these studies demonstrate that double-crosslinking strategies can markedly improve the mechanical and functional properties of hydrogels through tailored network architectures. However, most existing studies have focused primarily on improving bulk material properties, while less attention has been paid to how crosslinking design can be coordinated with the process-specific requirements of coaxial tubular printing. For hollow tubular printing, the material system must not only achieve sufficient post-crosslinking mechanical strength, but also satisfy rapid tube formation, shape retention during extrusion, and interfacial fusion between adjacent printed filaments or layers. Therefore, a double-network design that performs well in bulk hydrogel preparation does not necessarily translate directly into a suitable strategy for coaxial printing of hollow tubular scaffolds.

In this study, we developed a sequential ionic-covalent crosslinking strategy for the coaxial printing of hollow tubular scaffolds based on a sodium alginate (SA)/polyacrylamide double-network hydrogel system. In this strategy, ionic crosslinking of SA was first used to establish the primary tubular framework during printing, followed by acrylamide (AAm) polymerization under UV exposure in the presence of ammonium persulfate (APS) to reinforce the printed construct. This process-oriented design was intended to coordinate rapid hollow-tube formation, structural stabilization, and subsequent mechanical reinforcement within the same material system. In addition, the cytocompatibility of the fabricated scaffold was preliminarily evaluated through hydrogel leachate testing and perfusion-based culture of fibroblasts within the hollow tubes. The effects of crosslinking sequence, material composition, and printing parameters on scaffold morphology, microstructure, and mechanical performance were systematically investigated. The resulting tubular scaffolds showed improved mechanical robustness and acceptable cytocompatibility, demonstrating the feasibility of this strategy for in vitro tubular cell culture applications.

2. Materials and methods

2.1. Materials

The chemicals and biological materials used in this study were obtained from the following suppliers: SA and AAm were purchased from Kemiou Chemical Reagent Co., Ltd. (China); N,N'-methylenebisacrylamide (MBA) was supplied by Damao Chemical Reagent Factory (China); APS was obtained from Guanghua Technology Co., Ltd. (China); anhydrous calcium chloride ($CaCl_2$) was provided by Sinopharm Group Chemical Reagents Co., Ltd. (China). NIH/3T3 mouse embryonic fibroblasts and mouse embryonic fibroblast (MEF) cells were kindly provided by the State Key Laboratory for Conservation and Utilization of Subtropical Agro-bioresources at Guangxi University. Fibroblast culture medium (WISENT, China) and trypsin (Gibco, United States of America [USA]) were also used.

2.2. Preparation of hydrogel

A mixed solution of SA and AAm was prepared as the precursor. This precursor solution contained SA and AAm as the main components, with MBA as the covalent crosslinker and APS as the radical initiator for AAm polymerization. The AAm:SA, MBA:AAm, and APS:AAm weight ratios were 6:1, 0.006:1, and 0.01:1, respectively. The components were dissolved in ultrapure water under magnetic stirring to form a homogeneous mixture. Two types of hydrogels were prepared by altering the crosslinking sequence:

(i) CA-PAm hydrogel: Ionic crosslinking of SA with Ca^{2+} was performed first, followed by AAm polymerization under UV exposure in the presence of APS and MBA to form the covalent PAm network.
(ii) PAm-CA hydrogel: AAm polymerization was first carried out under UV exposure in the presence of APS and MBA to form the PAm network, followed by ionic crosslinking of SA with Ca^{2+}.

Both hydrogels were washed with ultrapure water to remove unreacted components. For performance testing, both bulk cylindrical hydrogels (27 mm in diameter) and filamentous hydrogels were prepared. The filaments were extruded using a syringe equipped with a 17-G metal needle. The wavelength of the UV light was 405 nm, the optical power was 699 mW, the distance between the sample and the UV source was 6–7 cm, and the irradiation time was two hours. Under the present formulation, APS was used as the radical initiator and MBA as the covalent crosslinker for AAm polymerization, whereas UV exposure was applied as the experimental condition for promoting reproducible formation of the PAm network.

2.3. Printing device and printing process

A custom coaxial printing system was assembled, consisting of a coaxial nozzle (inner needle: 20-G; outer needle: 14-G), a multi-channel injection pump, and a custom-built XY motion platform (Figure S6). The printing path is illustrated in Figure S7.

2.4. Mechanical testing

Tensile tests were performed using a UTM2502 universal testing machine (Haida Equipment, China) at a crosshead speed of 10 mm/min without preload. Each group was tested with at least three independent replicates, and the data are presented as mean ± standard deviation.

2.5. Fourier transform infrared spectroscopy and morphology observation

Fourier transform infrared spectroscopy (FTIR) spectra of PAm-CA and CA-PAm hydrogels were recorded using a Varian 640-IR spectrometer (Varian, USA) in the range of 400–4,000 cm^{-1}. For scanning electron microscopy (SEM) observation, hydrogel samples were freeze-dried, sectioned, sputter-coated with gold, and imaged under a scanning electron microscope (EVO 10, Zeiss, Germany) at 20 kV. Porosity was calculated using ImageJ software (NIH, USA) via the following steps: (i) converting SEM images to binary format; (ii) setting a threshold to separate pore areas from the hydrogel matrix; (iii) calculating the ratio of pore area to total image area. At least three representative SEM images were analyzed for each group.

2.6. Cell viability assay

NIH/3T3 cells were used for extract-based cytotoxicity screening, whereas MEF cells were used for direct perfusion culture in the hollow tubes to assess cytocompatibility in a tubular microenvironment. The hollow hydrogel tubes were rinsed thoroughly and immersed in ultrapure water for two days to obtain the leachate. NIH/3T3 cells were suspended in 1 mL of culture medium. They were cultured for 24 h at 37 °C in a 5% CO_2 atmosphere using medium with 10% fetal bovine serum. The cultured 3T3 cells were then detached using 0.25% trypsin-EDTA and subsequently seeded at a density of 3,500 cells/well into 96-well plates. The experimental design was summarized in Table 1.

Table 1. Experimental design for the hydrogel leachate cytotoxicity assay

Group	Cell seeding	Medium	Leachate added
A	NIH/3T3 cells	90 μL DMEM	10 μL
B	NIH/3T3 cells	100 μL DMEM	–
C	–	90 μL DMEM	10 μL
D	–	100 μL DMEM	–

Each group was tested in triplicate to ensure experimental reproducibility. All groups were cultured in a CO_2 incubator for 1 day. After aspirating the liquid from the 96-well plate, 10 μL of CCK-8 (5 mg/mL) reagent was added to each well, followed by continued incubation for

four hours. The absorbance at 450 nm was then measured using a microplate reader, and cell viability was calculated as follows:

$$\text{Cell viability}(\%) = \frac{\mathbf{A}_{\text{experimental group}} - \mathbf{A}_{\text{blank experimental group}}}{\mathbf{A}_{\text{control group}} - \mathbf{A}_{\text{blank control group}}} \times 100\%$$

For direct cell culture within tubes, MEF cells were inoculated into the hollow tubular hydrogel by perfusion and then cultured. The cells were harvested for live/dead staining observation after 3, 5, and 7 days of culture. Cell survival rates were quantified via ImageJ.

3. Results and discussion

3.1. Principle of 3D printing and dual-crosslinking

The principle of 3D printing and dual-crosslinking of hollow tubular scaffolds is shown in Figure 1. The hollow tubular structure was fabricated using coaxial extrusion-based 3D printing, with a SA/AAm composite solution as the outer flow and $CaCl_2$ solution as the inner flow. Upon extrusion, Ca^{2+} from the inner flow diffused into the SA/AAm in the outer flow, triggering ionic crosslinking of alginate and resulting in rapid gelation, forming the inner wall of the tube. To promote gelation of the outer wall, a low-concentration $CaCl_2$ solution was pre-deposited in the printing receiver. The scaffold was built layer-by-layer following a predefined path on an XY moving stage. Subsequently, the printed tubular structure was subjected to UV irradiation for two hours to promote AAm polymerization in the presence of APS and MBA, thereby forming a covalently crosslinked PAm network interpenetrating with the ionically crosslinked alginate network. This two-step process yielded a dual-network hydrogel tubular scaffold composed of an ionically crosslinked alginate network and a covalently crosslinked PAm network. After thorough washing, the scaffold was perfused with cell suspension to facilitate adhesion and culture of cells along the inner tube wall.

3.2. Effect of crosslinking sequence and material composition

Previously reported SA/AAm hydrogels are denoted here as PAm-CA hydrogels because they are commonly prepared by first forming the PAm network and then introducing ionic crosslinking of SA. In the present study, a CA-PAm hydrogel was designed in which alginate was ionically crosslinked before subsequent AAm polymerization under UV exposure. This sequential design was not intended as a simple change in preparation order, but as a process-oriented strategy to better match the requirements of coaxial tubular printing, where rapid hollow-tube formation, structural retention during deposition, and subsequent mechanical reinforcement must be coordinated within the same material system.

To clarify the respective roles of the two networks, hydrogels containing both SA and AAm were first prepared with only one network formed at a time, and their tensile properties were evaluated. As shown in Figure 2a, the hydrogel with only the PAm network formed exhibited substantially higher tensile strength and elongation

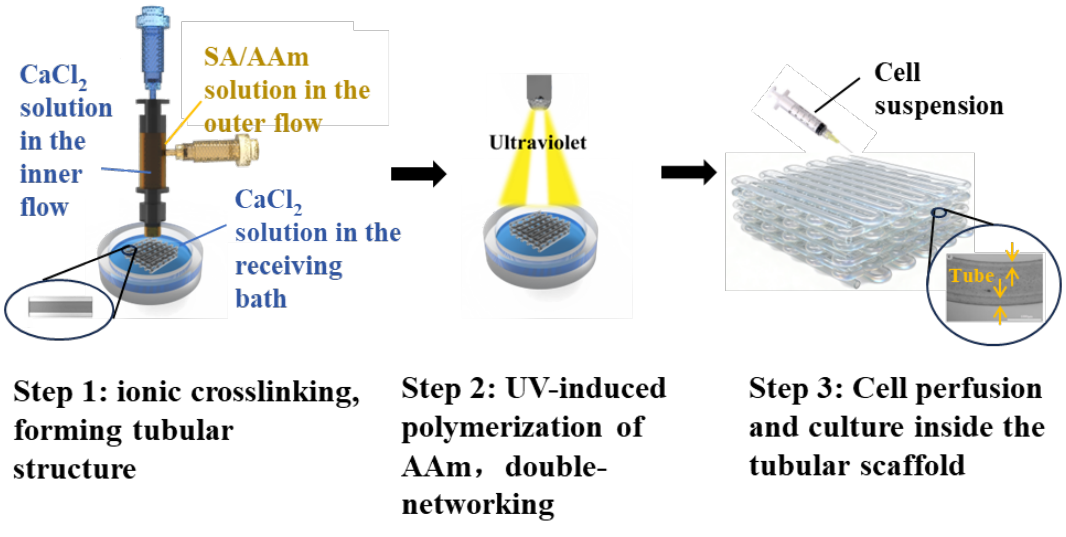

Figure 1. Schematic of the coaxial printing and sequential dual-crosslinking process for hollow tubular hydrogel scaffolds

at break than the hydrogel with only the Ca-alginate network. Under the present experimental conditions, the best single-network mechanical performance was obtained after two hours of UV exposure for PAm network formation and four hours of $CaCl_2$ immersion for alginate ionic crosslinking. These results indicate that the PAm network contributed more strongly to the final mechanical reinforcement. However, the alginate network was still essential in the present system because it could be formed rapidly during coaxial extrusion and thus establish the initial tubular framework before the subsequent covalent strengthening step.

As shown in Figure 2b, obvious morphological differences were observed between PAm-CA and CA-PAm hydrogels, and these differences became more pronounced at higher $CaCl_2$ concentration. For the PAm-CA hydrogel, the preformed PAm network acted as a mechanically constraining framework during the subsequent ionic crosslinking of SA, thereby limiting the dimensional shrinkage associated with alginate gelation and helping the hydrogel retain the original mold shape. In contrast, for the CA-PAm hydrogel, alginate ionic crosslinking occurred before formation of the PAm network, so the structure was able to undergo a more complete shrinkage and densification process during ionic gelation, especially at higher Ca^{2+} concentration. A plausible explanation for this asymmetry is that the preformed PAm network in PAm-CA mainly restricts the dimensional evolution of the system during subsequent alginate gelation, thereby reducing the extent of structural densification. By contrast, when alginate is ionically crosslinked first, the resulting network still contains water-rich domains and unpolymerized AAm monomers, allowing subsequent AAm polymerization to proceed within the pre-established ionic framework. In other words, the first-formed alginate network mainly determines the initial compactness of the hydrogel structure, whereas the subsequently formed PAm network mainly reinforces the preformed framework.

The mechanical results supported this interpretation. As shown in the stress-strain curves in Figure 2c and the tensile strength and elongation-at-break data in Figure S1a and S1b, CA-PAm hydrogels exhibited markedly higher tensile strength and elongation at break than PAm-CA hydrogels at the same $CaCl_2$ concentration. This enhancement is therefore more reasonably attributed to differences in network architecture generated by the crosslinking sequence, rather than to differences in chemical composition. In addition, increasing the $CaCl_2$

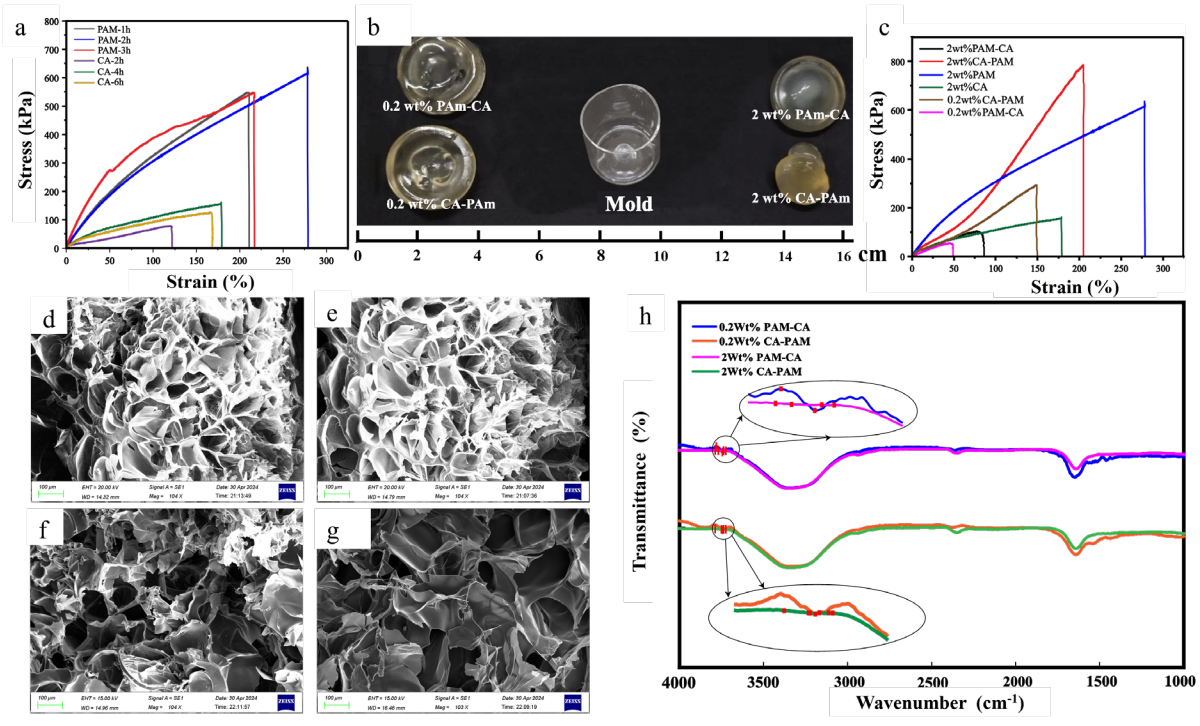

Figure 2. The influence of the crosslinking sequence and Ca^{2+} concentration on hydrogel morphology, microstructure, and mechanical properties. (a) Stress–strain curves of hydrogels with only one network formed; (b) Hydrogels prepared by two different crosslinking sequences; (c) Stress–strain curves of the hydrogels; (d–g) Scanning electron microscopy of the hydrogels (0.2 wt% $CaCl_2$ PAm-CA, 0.2 wt% $CaCl_2$ CA-PAm, 2 wt% $CaCl_2$ PAm-CA, 2 wt% $CaCl_2$ CA-PAm, respectively). Scale bar: 100 μm, magnification: 104×; (h) Fourier transform infrared spectra of the hydrogels.

concentration further intensified alginate ionic gelation, which was accompanied by improved compactness and enhanced mechanical performance.

To further verify the structural origin of this difference, the microstructure of the hydrogels was examined by SEM, as shown in Figure 2d–g. All samples exhibited interconnected porous structures. Porosity was quantified using ImageJ, and the calculated values were 37.211% and 51.217% for CA-PAm hydrogels crosslinked with 2 wt% and 0.2 wt% $CaCl_2$, respectively, compared with 43.448% and 55.825% for the corresponding PAm-CA hydrogels. These results indicated that CA-PAm hydrogels consistently possessed lower overall porosity than PAm-CA hydrogels under the same $CaCl_2$ condition, supporting the interpretation of a denser network structure. At 0.2 wt% $CaCl_2$, the hydrogels displayed flocculent network features with relatively high porosity, indicating a looser dried structure. At 2 wt% $CaCl_2$, the network became more sheet-like. Although some pores appeared larger in the SEM images, the number of pores decreased, and the overall porosity became lower, indicating that the dried network was, on the whole, more compact. This trend was more evident in the CA-PAm hydrogels. Therefore, the apparent increase in local pore size at higher $CaCl_2$ concentration should not be interpreted alone as evidence of a looser structure; rather, the overall compactness depends on the combined effects of pore number, pore-wall continuity, and total porosity.

To determine whether the crosslinking sequence changed the chemical structure of the hydrogels, FTIR spectra were measured and are shown in Figure 2h. No significant differences were observed between the spectra of PAm-CA and CA-PAm hydrogels, indicating that the crosslinking sequence did not alter the main chemical composition of the hydrogels. A minor difference was that, at 0.2 wt% $CaCl_2$, an O–H stretching peak appeared at 3,800–3,700 cm^{-1}, suggesting incomplete ionic crosslinking under insufficient Ca^{2+} conditions. Therefore, the observed differences in morphology and mechanical behavior are more reasonably attributed to sequence-dependent differences in network formation and structural evolution, rather than to changes in chemical identity.

From the perspective of coaxial tubular printing, these results suggest that the CA-PAm route is advantageous because it allows the alginate network to first establish the hollow tubular framework during extrusion, while the subsequent PAm network provides additional covalent reinforcement after printing. Accordingly, a relatively high $CaCl_2$ concentration in the inner flow is beneficial for the rapid formation of a dense and mechanically stable inner tube wall, whereas a lower $CaCl_2$ concentration in the receiving bath is favorable for slower outer-wall gelation, interfacial fusion between adjacent filaments, and stable multilayer structure formation.

3.3. Performance optimization of CA-PAm hydrogel

To achieve a suitable printing solution for CA-PAm hydrogels, the effects of SA, AAm, and $CaCl_2$ concentrations on hydrogel properties were systematically investigated. As shown in Figure 3a, a significant increase in the solution viscosity was observed when the SA concentration exceeded 2.5 wt%. In coaxial printing, excessively high viscosity leads to high printing pressure and risk of nozzle clogging. Conversely, excessively low viscosity increases the difficulty of controlling printing parameters. Therefore, an SA concentration of 2.5 wt% was selected, providing suitable viscosity for coaxial printing. The influence of AAm concentration on the mechanical properties of the hydrogel is shown in Figure 3b. When the AAm concentration increased from 10 wt% to 20 wt%, both the tensile strength and elongation at break initially increased and then decreased. At lower AAm concentrations, the number of AAm molecules available for crosslinking under UV irradiation was limited. As the AAm content increased, more molecules participated in covalent crosslinking, enhancing the strength of the PAm network. However, beyond an optimal point, excessive crosslinking reduced molecular chain mobility, leading to stress concentration and ultimately a decline in mechanical properties. The optimal AAm concentration was found to be 15 wt%, yielding a tensile strength of 809.80 kPa and an elongation at break of 217.07%. The concentration of $CaCl_2$ significantly influenced the crosslinking kinetics, thereby affecting the microstructure and properties of the hydrogel. As shown in Figure 3c and 3d, at low $CaCl_2$ concentrations, both tensile strength and elongation at break increased with $CaCl_2$ due to enhanced ionic crosslinking between Ca^{2+} ions and SA chains. At higher concentrations, these properties initially improved, then decreased beyond 2 wt% $CaCl_2$. Excessive Ca^{2+} ions accelerated gelation, leading to a heterogeneous network with localized stress points, thereby compromising mechanical performance.

3.4. Optimization of printing parameters

In addition to the ink composition, printing parameters are also critical factors influencing the morphology of tubular structures. The experimental results indicated that printing parameters not only determined the inner diameter and wall thickness of the tube, but also significantly affected the interfacial fusion between adjacent layers, thereby influencing the overall structural integrity and dimensional accuracy. As shown in Figure 4a, when the inner flow rate was fixed at 0.5 mL/min, and the outer flow

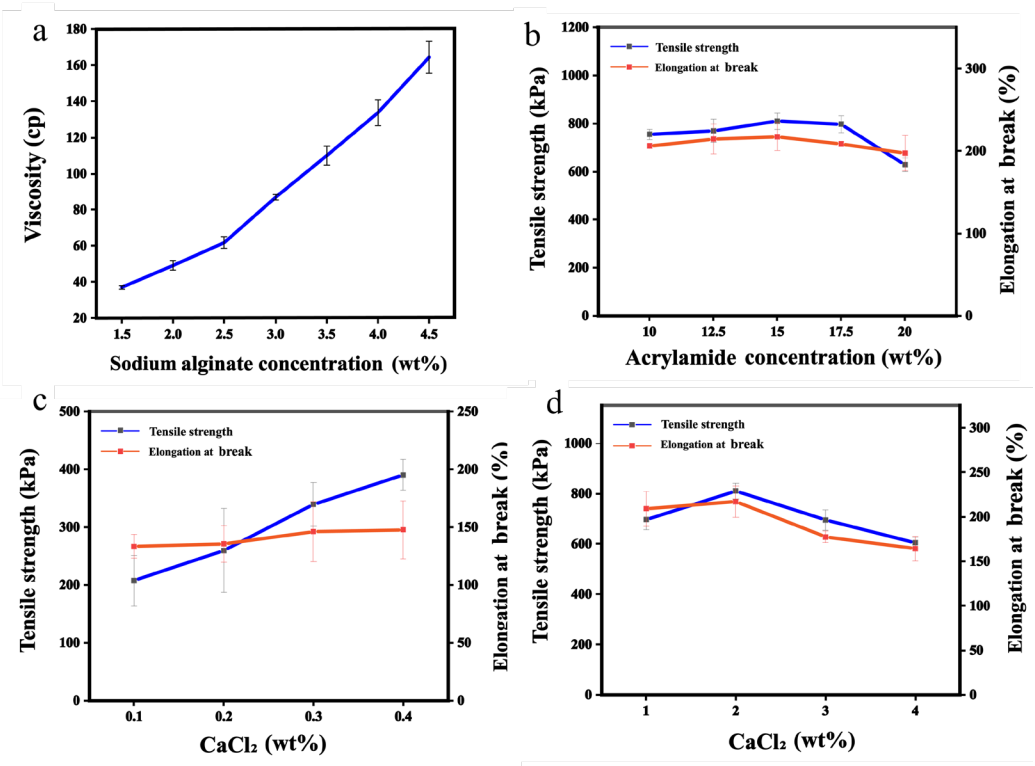

Figure 3. (a) Viscosity curve of the ink; (b) The effect of AAm concentration on tensile properties; (c) Effect of low concentration $CaCl_2$ on tensile properties; (d) Effect of high concentration of $CaCl_2$ on tensile properties

rate varied from 0.2 to 0.5 mL/min, the inner diameter of the tube slightly increased with the outer flow rate, while the wall thickness initially decreased and then increased. The reduced velocity difference between the inner and outer streams resulted in smaller mechanical confinement from the outer flow onto the inner flow, slightly enlarging the inner diameter.[23] At the same time, the increase in outer flow rate increased the outer diameter, but the rate of increase of the inner and outer diameter was different, resulting in a non-monotonic change in wall thickness. As shown in Figure 4b, when the outer flow rate was fixed at 0.2 mL/min, and the inner flow rate varied from 0.5 to 2 mL/min, the inner diameter of the tube increased with higher inner flow rates, while the wall thickness consistently decreased. This was because the inner flow exerted greater pressure on the outer flow, expanding the inner diameter and reducing the wall thickness.[24] As shown in Figure 4c, the wall thickness of the tube generally decreased as the inner-to-outer flow rate ratio increased. The maximum wall thickness of approximately 0.254 mm was achieved when the flow rate ratio was 1:1.

As shown in Figure 5a, the platform moving speed significantly influenced the morphology of the extracted filament, thereby affecting the tubular structure. With the inner flow rate fixed at 0.5 mL/min and the outer flow rate varied between 0.2 and 0.5 mL/min, the platform moving speed was gradually increased to observe the filament formation to determine the applicable range of printing speeds. The results were summarized in Figure 5b. It was found that when the platform speed was less than eight times the outer flow rate, the printed hollow tubes exhibited distortion and rough surfaces due to material accumulation. At platform moving speeds between 8 and 18 times the outer flow rate, the hollow tubes formed with smooth surfaces and no obvious distortion, indicating optimal speed matching. When the platform's moving speed exceeded 18 times the outer flow rate, the excessive speed caused dragging and deviation from the intended printing path, resulting in printing failure. As shown in Figure 5c, the concentration of the $CaCl_2$ solution also played a critical role in the formation of 3D structures. An excessively high $CaCl_2$ concentration in the receiving bath accelerated the gelation of the outer wall, preventing proper fusion between adjacent tube layers. Based on these findings and previous material properties, the optimal concentrations

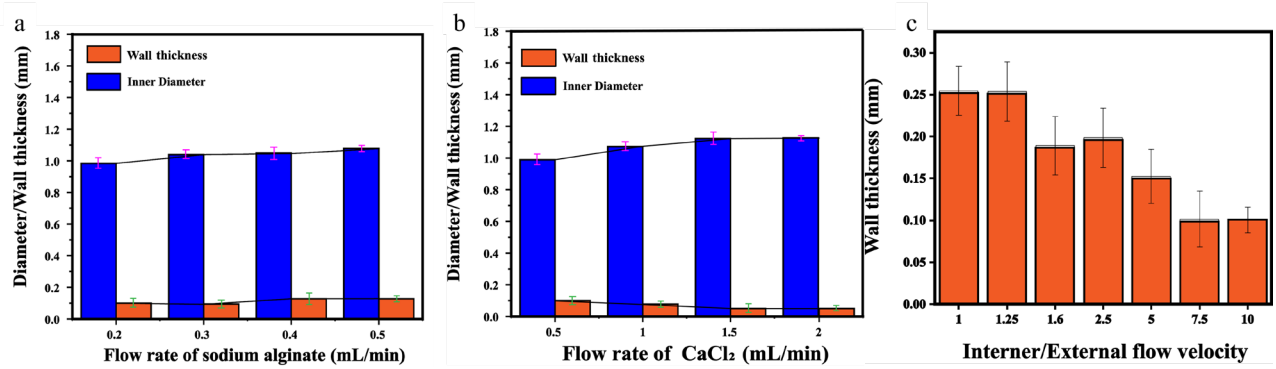

Figure 4. (a) The influence of outer flow rate on the inner diameters and tube wall thickness; (b) The influence of inner flow rate on the inner diameters and tube wall thickness; (c) The influence of inner-outer flow rate ratios on the wall thickness

were selected as 2 wt% $CaCl_2$ for the inner flow and 0.2 wt% for the receiving bath. Using the optimized printing parameters, a 3D structure was successfully fabricated, as shown in Figure 5d. The structure consisted of hollow tubes arranged in a serpentine pattern with adjacent layers staggered at 90°. Microscopic examination confirmed the alternating 90° stacking between layers in the multilayer architecture. Representative images confirming intact hollow tubular scaffolds are shown in Figure S2.

3.5. Biological performance

To evaluate the potential of the printed tubular scaffolds for tissue engineering applications, the biological performance was assessed through cell viability tests. NIH/3T3 mouse embryonic fibroblasts were used for the hydrogel leachate cytotoxicity assay, whereas MEF cells were used for perfusion culture within the hollow tubular scaffold. The experimental design is shown in Table 1. As shown in the bright-field images in Figure 6a and 6b, no significant differences in cell morphology or density were observed between the control and experimental groups, indicating that the leachate of the hydrogel did not adversely affect cell attachment or proliferation. NIH/3T3 mouse embryonic fibroblasts were selected for CCK-8 cytotoxicity testing as they are a widely recognized model for in vitro biocompatibility evaluation with stable growth characteristics, suitable for preliminary toxicity screening of hydrogel leachate. The absorbance at 450 nm and the corresponding cell viability values calculated from the CCK-8 assay are shown in Figure 6c. Group A evaluates the cytotoxicity of hydrogel leachate by co-culturing NIH/3T3 cells with leachate; Group B reflects normal cell growth without leachate interference; Group C excludes cells to verify that leachate does not affect medium absorbance; Group D excludes both cells and leachate to eliminate background absorbance from DMEM alone. No significant difference in absorbance was detected between Groups C and D. The cell viability values in Group A were 86.7%, 93.2%, and 89.6%, giving a mean value of 89.8 ± 3.3%. These results demonstrated that the hydrogel leachate supports high cell viability, exceeding 85%, and confirmed the good biocompatibility of the fabricated scaffolds.

Mouse embryonic fibroblasts were used for perfusion culture within the tubular scaffold as a model cell line to preliminarily evaluate cytocompatibility in the hollow tubular microenvironment. A cell suspension containing MEF was perfused into the hollow tubes and cultured under standard conditions. The results were presented in Figures 7 and S3–S5. Quantitative analysis revealed that the cell survival rate within the hollow tubes was 85.4% after 3 days, 70.9% after 5 days, and 58.0% after 7 days. Compared with the previously reported 7-day survival rate (50.2 ± 1.6%) for cells cultured in a CA hydrogel mixed system,[25,26] the CA-PAm hydrogel tubular structure maintained a higher survival rate of approximately 60% at the same time point. These results indicate low cytotoxicity and acceptable cytocompatibility of the hydrogel during the culture period.

4. Conclusion

In this study, a dual-crosslinked hollow tubular hydrogel scaffold was successfully fabricated by coaxial extrusion-based printing using a SA/AAm system. Compared with the conventional PAm-CA route, the CA-PAm route, in which alginate ionic crosslinking preceded AAm

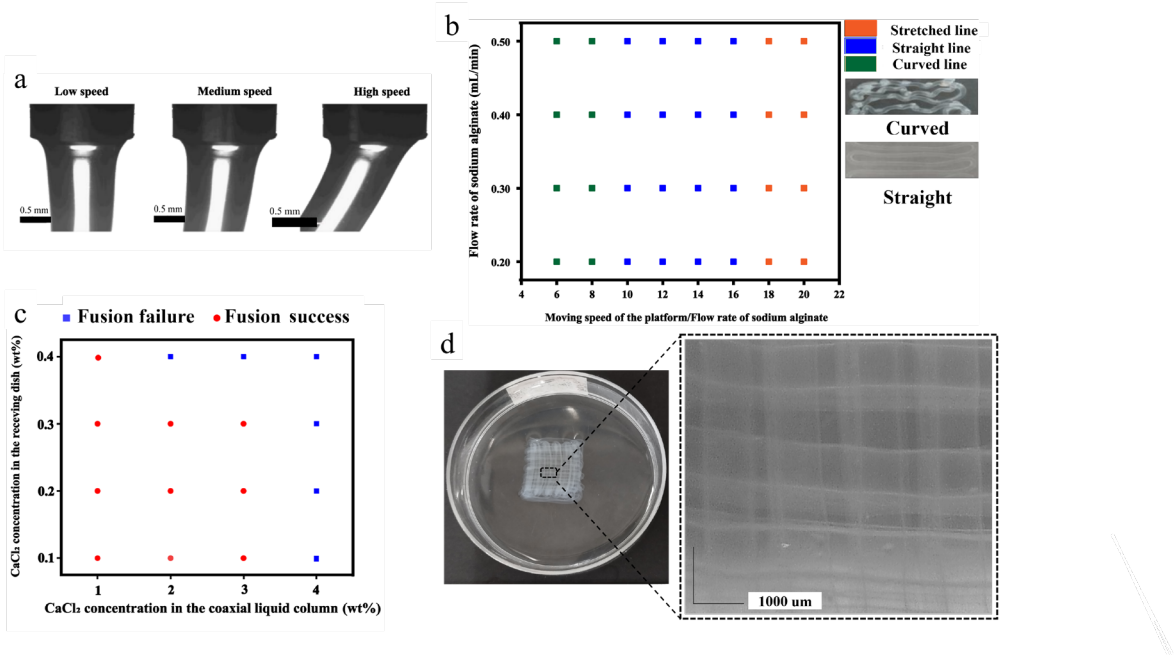

Figure 5. (a) Filament morphology at different platform speeds; (b) Effect of platform speed on single-layer structure formation; (c) Effect of $CaCl_2$ concentration on multilayer fusion; (d) Macroscopic and microscopic images of the multilayer tubular structure. Scale bars: 1,000 μm; magnification: 20×.

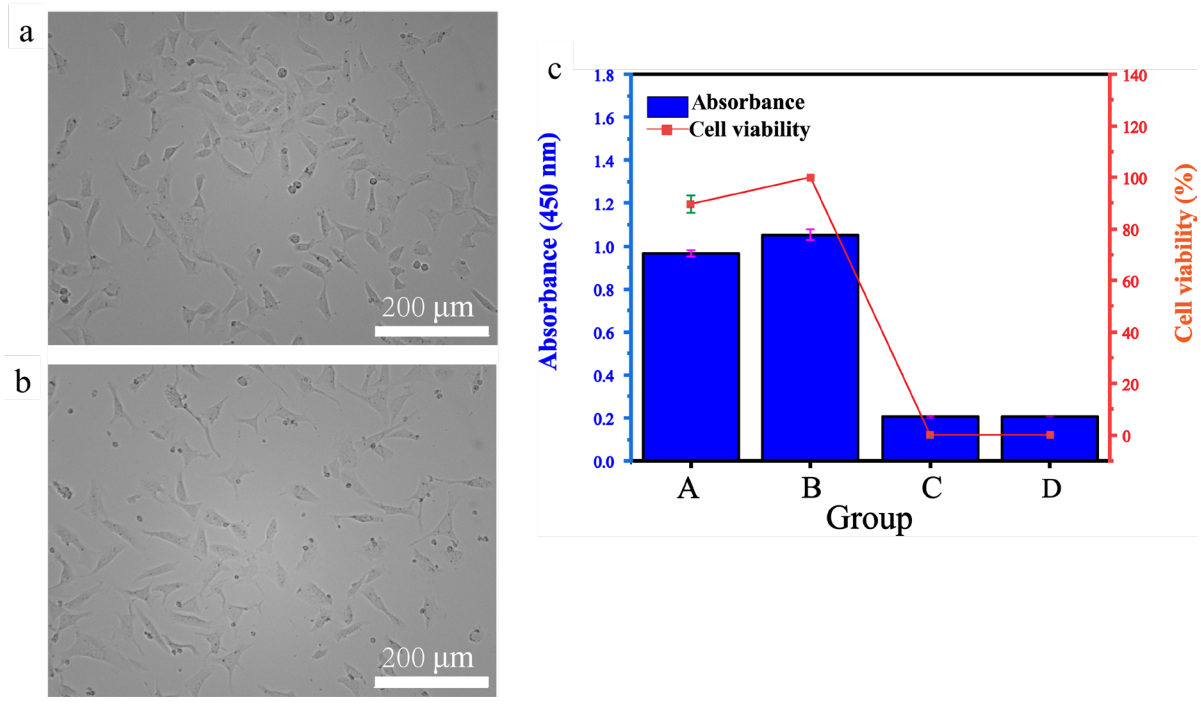

Figure 6. Detection of CCK-8 cell activity in hydrogel leachate: (a) Light microscopy of cells in Group B. Scale bars: 200 μm; magnification: 40×; (b) Light microscopy of cells in Group A. Scale bars: 200 μm; magnification: 40×; (c) CCK-8 test results.

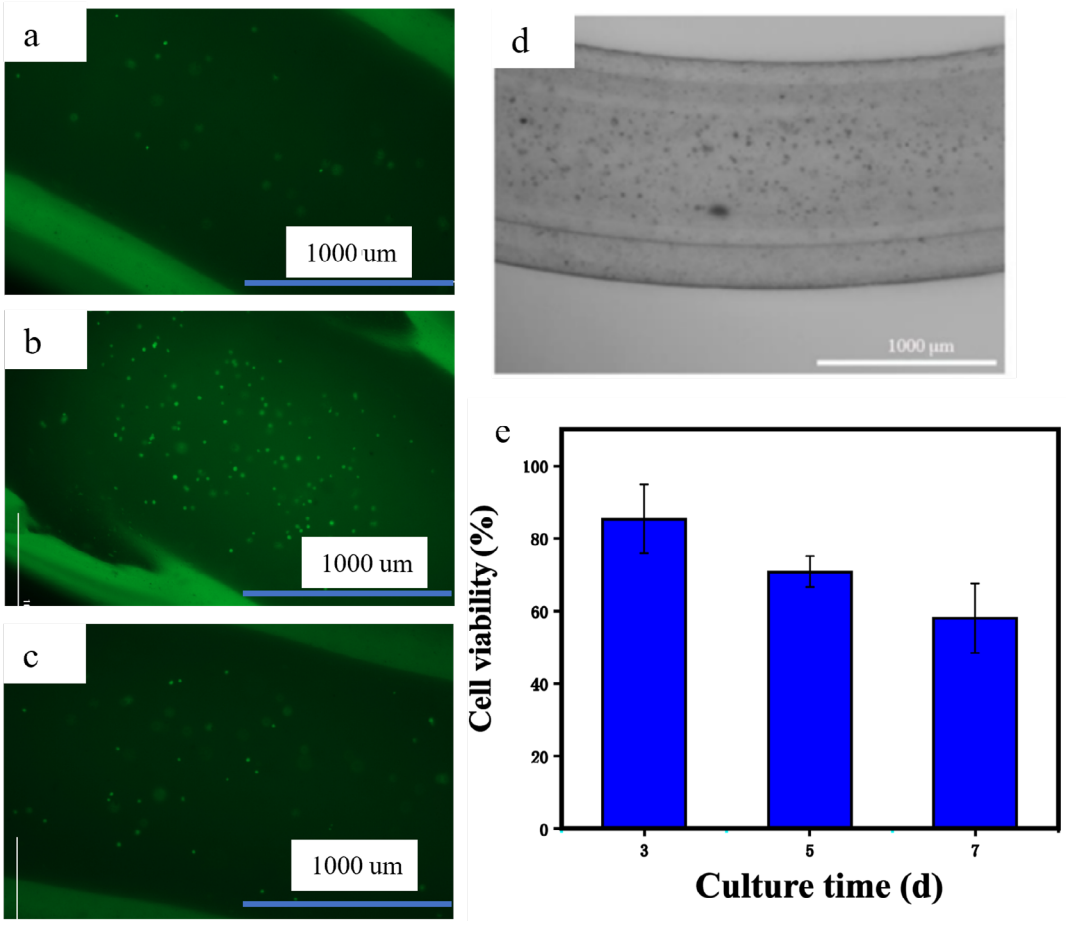

Figure 7. Live-cell fluorescence images of mouse embryonic fibroblast (MEF) cells in hollow tubes. (a–c) Green-fluorescence images of live cells after 3, 5, and 7 days of culture. Scale bars: 1,000 μm; magnification: 20×; (d) bright-field image of cell perfusion within the hollow tube. Scale bars: 1,000 μm; magnification: 20×; (e) MEF cell survival rate.

polymerization, produced a denser network structure and better mechanical performance without changing the main chemical composition of the hydrogel. The results indicate that the crosslinking sequence primarily regulates network formation and structural evolution. The superior performance of CA-PAm is attributed to early structural compaction during alginate gelation, followed by subsequent reinforcement from the PAm network, supported by the single-network controls, SEM observations, porosity analysis, and FTIR results. When the SA concentration was 2.5 wt%, and the AAm concentration was 15 wt%, the CA-PAm hydrogel achieved a tensile strength of 809.80 kPa and an elongation at break of 217.07%. In the printing process, the tube wall thickness was mainly determined by the inner-to-outer flow rate ratio, while stable tube formation was obtained when the platform moving speed was 8–18 times the outer flow rate. In addition, the CaCl2 concentration in the receiving bath significantly affected interlayer fusion and thus the structural stability of the printed construct. Biological evaluation showed good biocompatibility, with a cell viability of 89.8% in the leachate assay and a 3-day cell survival rate of 85.4% within the tubular scaffold. These findings show that crosslinking-sequence reconfiguration is a practical strategy for matching material gelation behavior with the demands of coaxial tubular printing and provide a feasible route for fabricating mechanically robust and cytocompatible hollow hydrogel scaffolds for tissue engineering.

Acknowledgments

None.

Funding

The authors thank the support of Guangxi Young Elite

Scientists Sponsorship Program (GXYESS2025029), Natural Science Foundation of Guangxi Province (2025GXNSFAA069620), and National Natural Science Foundation of China (52005115).

Conflict of interest

The authors declare they have no competing interests.

Author contributions

Conceptualization: Yuanfen Chen, Ben Huang
Formal analysis: Wenle Yu, Dingjian Liang, Renzhi Wang, Yuanfen Chen, Ben Huang
Investigation: Wenle Yu, Dingjian Liang
Methodology: Wenle Yu, Dingjian Liang, Renzhi Wang, Jingyao Gai, Quanhui Liu
Writing–original draft: Wenle Yu, Dingjian Liang, Yuanfen Chen, Ben Huang
Writing–review & editing: Yuanfen Chen, Ben Huang

Ethics approval and consent to participate

Not applicable.

Consent for publication

Not applicable.

Availability of data

Data is available from the corresponding author upon reasonable request.

References

1. Khademhosseini A, Langer R. A decade of progress in tissue engineering. *Nat Protoc*. 2016;11(10):1775-1781.

   doi: 10.1038/nprot.2016.123

2. Rouwkema J, Rivron NC, van Blitterswijk CA. Vascularization in tissue engineering. *Trends Biotechnol*. 2008;26(8):434-441.

   doi: 10.1016/j.tibtech.2008.04.009

3. Ntege EH, Sunami H, Shimizu Y. Advances in regenerative therapy: A review of the literature and future directions. *Regen Ther*. 2020;14:136-153.

   doi: 10.1016/j.reth.2020.01.004

4. Kolesky DB, Homan KA, Skylar-Scott MA, Lewis JA. Three-dimensional bioprinting of thick vascularized tissues. *Proc Natl Acad Sci USA*. 2016;113(12):3179-3184.

   doi: 10.1073/pnas.1521342113

5. Zhu W, Qu X, Zhu J, *et al*. Direct 3D bioprinting of prevascularized tissue constructs with complex microarchitecture. *Biomaterials*. 2017;124:106-115.

   doi: 10.1016/j.biomaterials.2017.01.042

6. Priya SG, Jungvid H, Kumar A. Skin Tissue Engineering for Tissue Repair and Regeneration. *Tissue Eng Part B Rev*. 2008;14(1):105-118.

   doi: 10.1089/teb.2007.0318

7. Ratcliffe A. Tissue engineering of vascular grafts. *Matrix Biol*. 2000;19(4):353-357.

   doi: 10.1016/s0945-053x(00)00080-9

8. Mollica PA, Booth-Creech EN, Reid JA, *et al*. 3D bioprinted mammary organoids and tumoroids in human mammary derived ECM hydrogels. *Acta Biomater*. 2019;95:201-213.

   doi: 10.1016/j.actbio.2019.06.017

9. Xue L, Greisler HP. Biomaterials in the development and future of vascular grafts. *J Vasc Surg*. 2003;37(2):472-480.

   doi: 10.1067/mva.2003.88

10. Datta P, Ayan B, Ozbolat IT. Bioprinting for vascular and vascularized tissue biofabrication. *Acta Biomater*. 2017;51:1-20.

    doi: 10.1016/j.actbio.2017.01.035

11. Jain RK, Au P, Tam J, Duda DG, Fukumura D. Engineering vascularized tissue. *Nat Biotechnol*. 2005;23(7):821-823.

    doi: 10.1038/nbt0705-821

12. Boland T, Xu T, Damon B, Cui X. Application of inkjet printing to tissue engineering. *Biotechnol J*. 2006;1(9):910-917.

    doi: 10.1002/biot.200600081

13. Boland T, Mironov V, Gutowska A, Roth EA, Markwald RR. Cell and organ printing 2: Fusion of cell aggregates in three-dimensional gels. *Anat Rec*. 2003;272A(2):497-502.

    doi: 10.1002/ar.a.10059

14. Gu BK, Choi DJ, Park SJ, Kim YJ, Kim CH. 3D Bioprinting Technologies for Tissue Engineering Applications. In: *Advances in Experimental Medicine and Biology*. Springer Singapore; 2018:15-28.

    doi: 10.1007/978-981-13-0950-2_2

15. Duan B, Hockaday LA, Kang KH, Butcher JT. 3D Bioprinting of heterogeneous aortic valve conduits with alginate/gelatin hydrogels. *J Biomed Mater Res A*. 2013;101A(5):1255-1264.

    doi: 10.1002/jbm.a.34420

16. Albrecht DR, Underhill GH, Wassermann TB, Sah RL, Bhatia SN. Probing the role of multicellular organization in three-dimensional microenvironments. *Nat Methods*. 2006;3(5):369-375.

    doi: 10.1038/nmeth873

17. Khalil S, Sun W. Bioprinting Endothelial Cells With Alginate for 3D Tissue Constructs. *J Biomech Eng*. 2009;131(11):111002.

    doi: 10.1115/1.3128729

18. Attalla R, Puersten E, Jain N, Selvaganapathy PR. 3D bioprinting of heterogeneous bi- and tri-layered hollow channels within gel scaffolds using scalable multi-axial microfluidic extrusion nozzle. *Biofabrication*. 2018;11(1):015012.

doi: 10.1088/1758-5090/aaf7c7

19. Shao L, Gao Q, Xie C, Fu J, Xiang M, He Y. Directly coaxial 3D bioprinting of large-scale vascularized tissue constructs. *Biofabrication*. 2020;12(3):035014.

doi: 10.1088/1758-5090/ab7e76

20. Pei M, Peng X, Wan T, *et al*. Double cross-linked poly(vinyl alcohol) microcomposite hydrogels with high strength and cell compatibility. *Eur Polym J*. 2021;160:110786.

doi: 10.1016/j.eurpolymj.2021.110786

21. E S, Ning D, Wang Y, *et al*. Ternary Synergistic Strengthening and Toughening of Bio-Inspired TEMPO-Oxidized Cellulose Nanofibers/Borax/Polyvinyl Alcohol Composite Film with High Transparency. *ACS Sustainable Chem Eng*. 2020;8(41):15661-15669.

doi: 10.1021/acssuschemeng.0c05292

22. Zhong Y, Lin Q, Yu H, *et al*. Construction methods and biomedical applications of PVA-based hydrogels. *Front Chem*. 2024;12.

doi: 10.3389/fchem.2024.1376799

23. Sun JY, Zhao X, Illeperuma WRK, *et al*. Highly stretchable and tough hydrogels. *Nature*. 2012;489(7414):133-136.

doi: 10.1038/nature11409

24. Zhang Y, Yu Y, Chen H, Ozbolat IT. Characterization of printable cellular micro-fluidic channels for tissue engineering. *Biofabrication*. 2013;5(2):025004.

doi: 10.1088/1758-5082/5/2/025004

25. Gao Q, He Y, Fu J-z, Liu A, Ma L. Coaxial nozzle-assisted 3D bioprinting with built-in microchannels for nutrients delivery. *Biomaterials*. 2015;61:203-215.

doi: 10.1016/j.biomaterials.2015.05.031

26. Jia W, Gungor-Ozkerim PS, Zhang YS, *et al*. Direct 3D bioprinting of perfusable vascular constructs using a blend bioink. *Biomaterials*. 2016;106:58-68.

doi: 10.1016/j.biomaterials.2016.07.038